Incremental Nonlinear Dynamic Inversion control with Flight Envelope Protection for the Flying-V

Stougie, P.J.; Pollack, T.S.C.; van Kampen, E.

DOI
10.2514/6.2024-2565

Publication date
2024

Document Version
Final published version

Published in
Proceedings of the AIAA SCITECH 2024 Forum

AIAA SciTech Forum
8-12 January 2024, Orlando, FL
AIAA SCITECH 2024 Forum

10.2514/6.2024-2565

Incremental Nonlinear Dynamic Inversion control with Flight Envelope Protection for the Flying-V

Jurian Stougie * Tijmen Pollack† Erik-Jan van Kampen‡
Faculty of Aerospace Engineering, Delft University of Technology, Delft, 2629HS, The Netherlands

To reduce the impact of aviation on the environment, technological innovations, such as the Flying-V are required. The Flying-V is a proposed commercial flying wing, which uses the Airbus A350-900 as reference aircraft. In this work, a Flight Control system for the Flying-V is proposed with a longitudinal C^* control law, and a Rate Control Attitude Hold roll control law. This Flight Control System also includes a Flight Envelope Protection law to prevent reaching angles of attack higher than 30 degrees, where the Flying-V becomes statically unstable. The FEP also prevents the Flying-V from reaching load factors above 2.5 and limits the roll angle. The control laws are tuned to be within level 1 handling qualities in the selected approach and cruise conditions, with the presence of sensor dynamics, and a digital control system. Robustness for aerodynamic uncertainties is also shown. Finally, it is shown that the FEP is able to prevent the angle of attack from becoming too large.

I. Introduction

In 2010 around, 4.9 % of the radiative forcing, causing climate change, comes from aviation, and this is projected to increase 3-4 times in 2050 [1]. To reduce the impact of aviation on the environment, technological innovations are required. The Flying-V is a possible way of reducing the environmental impact of aircraft, as research shows that the Flying-V could be up to 25 % percent more aerodynamically efficient than conventional aircraft [2].

The Flying-V was first proposed by Benad [3] in 2015 as a commercial flying wing. The Airbus A350-900 was used as a reference aircraft [3]. It was designed to have a capacity of 315 passengers, and a cruise speed of Mach 0.85, which is the same as the Airbus reference aircraft.

However, research also showed that the Flying-V has some stability and control characteristics that need extra attention before it can be used as a commercial airliner. It suffers from pitch break-up for angles of attack above 20 degrees [4]. It also has an unstable dutch roll in approach conditions [5] and low lateral control authority [6]. To increase the flying qualities of an aircraft, a Flight Control System can be implemented. Van Overeem [7] proposes a FCS based on Incremental Nonlinear Dynamic Inversion (INDI). This showed that the control laws were able to get the eigenmodes within level 1 handling qualities, however different effects that typically degrade the performance of the control system, such as time delays and sensor noise, were not taken into account. To get the Flying-V certified either the pitch break-up behaviour should be removed by redesigning the airframe, or some form of flight envelope protection should be implemented, to prevent from reaching angles of attack where the pitch break up becomes unrecoverable.

In this research the proposed FCS that is based on INDI will be extended. INDI, originally called Simplified NDI [8] is a nonlinear sensor-based control method, that requires less model information than, for example, Nonlinear Dynamic Inversion, and is therefore more robust for parametric uncertainties [9]. However, a difference in time delay between the actuator position and angular rate measurements typically degrades the performance of the INDI controller [10].

The goal of this research is to increase the maturity of the Flight Control System of the Flying-V, by evaluating the performance of the FCS with the effects of sensor dynamics, discretization, and aerodynamic uncertainties, as well as implementing a Flight Envelope Protection control law.

The structure of the paper is as follows. In section II the simulation model that will be used is explained,by first showing the aerodynamic model of the Flying-V and then the sensor and discrete time modeling are explained. Next, in section III the control laws of the FCS are given. After this in section IV the method of evaluating the control laws performance is given. Next, in section V the results of the research are presented and discussed. Finally, the conclusion is shown and recommendations for further research are given in section VI.

*MSc Student, Control and Simulation, Delft University of Technology
†PhD Student, Control and Simulation, Delft University of Technology
‡Assistant Professor, Control and Simulation, Delft University of Technology

II. Simulation model

In this section, the simulation model that is used for analysis is explained. First, the aerodynamic model of the Flying-V that will be used is presented. Then the way the discretization will be modeled is presented in section II.B, and the sensors in section II.C. Finally, in section IV.B the method of measuring the performance of the control laws is introduced.

A. Flying-V

The general layout of the Flying-V, with the locations of the control surfaces, can be seen in figure 1. A top-view of the wing, with exact inboard (δ_{CS_1}) and outboard (δ_{CS_2}) control surface dimensions is given in figure 2. The rudders (δ_{CS_3}) are integrated into the wing tips. The layout of the Flying-V is taken from the research of Cappuyns [5]. In this research, the forward centre of gravity will be used, which is located 29.4 m behind the nose. The analysis of the flight control system will be done in cruise and approach conditions. Cruise condition is on an altitude of 13 km at Mach 0.85, whereas in approach conditions the altitude is at sea level, with Mach 0.2. The mass of the aircraft is set to 240,000 kg.

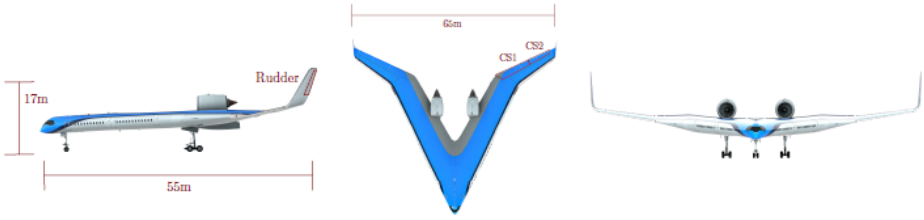

Fig. 1 Flying-V with control surface locations, retrieved from van Overeem [11]

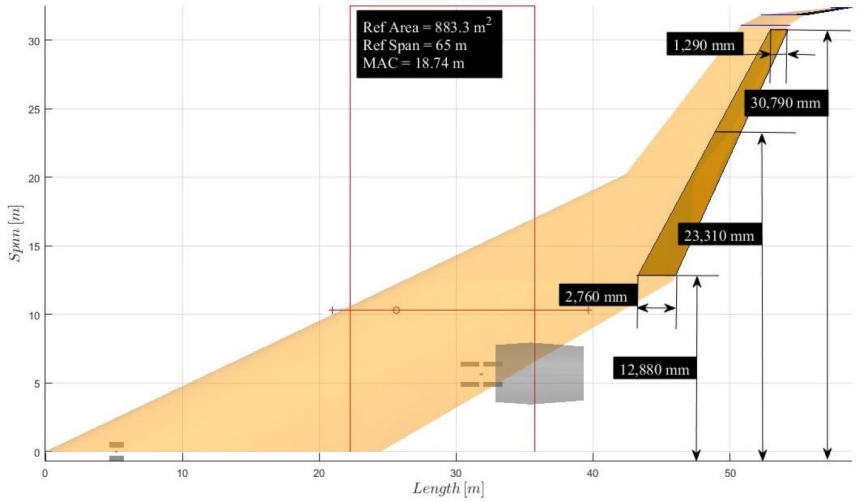

Fig. 2 Flying-V wing, from Cappuyns [5]

1. Aerodynamic model

The aerodynamic data used for this research is also as used by van Overeem [11]. This data is a combination of Vortex-Lattice Method (VLM) data obtained by Cappuyns [5] and Windtunnel data obtained by Garcia [12]. The VLM data is used as a baseline, which is the reason the control surface layout of this model is also used [11]. The longitudinal coefficients for angles of attack under 15 degrees are from the VLM model, whereas the data for angles of attack up to 30 degrees are from the wind tunnel data.

The aerodynamic coefficients are available for two Mach numbers (0.2 and 0.85). As some simulations will have a large variation of airspeed, the aerodynamic data is linearly interpolated between these two Mach numbers. The

aerodynamic data does not include compressibility effects. For the simulations, zero wind will be assumed. Furthermore, an atmosphere corresponding to the International Standard Atmosphere will be assumed.

2. Control Surfaces

To increase the flexibility of the control surfaces, the inboard and outboard control surfaces are split up in a left and right control surfaces, which can be directed independently from each other by the control allocation. The actuators are modeled as a second-order transfer function, given in equation 1, for which the values are obtained from Matamoros [13].

$$H_{act} = \frac{\omega_{act}^2}{s^2 + 2\zeta_{act}\omega_{act}s + \omega_{act}^2} = \frac{4000}{s^2 + 140s + 4000} \quad \text{and} \quad H_{thrust} = \frac{1}{0.2s + 1} \tag{1}$$

The rate limit for δ_{CS_1} and δ_{CS_2} is 80 deg/s and for δ_{CS_3} it is 120 deg/s. The position limits are 25 and 30 degrees respectively [5]. The thrust transfer function that converts the commanded thrust to actual thrust is given in equation 1 with the maximum thrust being $3.79 \cdot 10^5$ N [14].

B. Discrete-time modeling

The controller itself will run with a baseline sampling frequency of 100 Hz, and each sensor will have its own sampling frequency. The actuator dynamics as well as the aircraft dynamics will stay a continuous time system. In figure 4 an overview is given of which part of the simulation will run in which time frame. The discrete INDI control law is given in equation 2 [15]. The integrators in the controller will be replaced with discrete integrators using Tustins approximation, as given in equation 3 [16].

$$\boldsymbol{u}_k = \boldsymbol{u}_{k-1} + G^{-1}(\boldsymbol{x}_{k-1})\left(\boldsymbol{v}_k - \frac{\boldsymbol{x}_{k-1} - \boldsymbol{x}_{k-2}}{T_s}\right) \tag{2}$$

$$\frac{1}{s} \approx \frac{T_s(z+1)}{2(z-1)} \tag{3}$$

The signals will be sampled before and after the sensors, to get the discrete signals for the sensor and controller dynamics. Before the actuator and the engine dynamics, the signals will be converted back to continuous-time by a zero-order hold. This zero-order hold and sampler will be approximated with equation 4 for the linearized models [16].

$$G_{0_s}(s) = \frac{1 - e^{-sT_s}}{sT_s} \approx \frac{1 - sT_s/6}{1 + sT_s/3} \tag{4}$$

In MATLAB Simulink, zero-order hold blocks are used to sample signals, and signals are automatically converted to continuous time signals if required. Therefore for the nonlinear simulations, the sampling will be done with zero-order hold blocks, and no zero-order block will be used for transforming the signal from discrete to continuous time.

C. Sensor Modeling

The general overview of how the sensors will be modeled can be found in Figure 3. The baseline values for each sensor can be found in table 1. These values are based on values found by Grondman [17] for the sensors of the Cessna Citation II PH-LAB laboratory aircraft. The noise and bias are implemented by adding white noise to the signal, with a mean of the bias, and a standard deviation of the noise level. If the FCS cannot be tuned for level 1 Flying qualities with these values, the sensor(s) that prevent this should be identified, as well as the values for which level 1 can be obtained.

To obtain the angular accelerations, the output of the body rate filters is first filtered by a second order filter with a frequency of 30 rad/s and a damping ratio of 1 and then differentiated. The instantaneous change of pitch angle $\dot{\theta}$ and change of roll angle $\dot{\phi}$ are calculated using the gyroscopes.

It is assumed that the air density and actuator positions are at all times known by the controller, without any time delay, bias, or noise.

Table 1 Baseline sensor parameters, based on Grondman [17]

Sensor	Sampling rate $[hz]$	Time delay [s]	Noise	Bias	Filter time constant
p, q, r $[rad/s]$	50	0.1	$1 \cdot 10^{-9}$	$3 \cdot 10^{-5}$	0.05
ϕ, θ $[rad]$	50	0.1	$1 \cdot 10^{-9}$	$4 \cdot 10^{-3}$	0.05
V $[m/s]$	1/0.065	0.325	$1 \cdot 10^{-4}$	2.5	0.05
α, β $[rad]$	50	0.1	$7.5 \cdot 10^{-8}$	$3 \cdot 10^{-5}$	0.05
A_x, A_y, A_z $[g]$	50	0.1	$1 \cdot 10^{-5}$	$2.5 \cdot 10^{-3}$	0.05

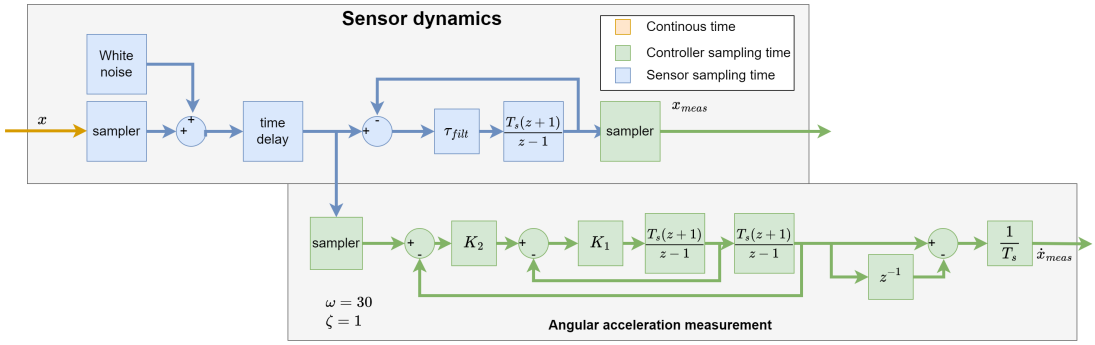

Fig. 3 Sensor dynamics model

III. Control laws

A. Incremental Nonlinear Dynamic Inversion and Control Allocation

The inner loop of the Flight control system will be based on an Incremental Nonlinear Dynamic Inversion (INDI) control law, which is extended with a control allocation algorithm, to ensure efficient use of the control surfaces.

1. INDI

For INDI it is assumed that you can describe the equations of motion as a system given in equation 5. In this equation $\boldsymbol{x}$ is the state vector, $\boldsymbol{u}$ the input vector, and $\boldsymbol{y}$ the output vector. To this system a Taylor expansion is applied, where higher order terms are neglected [10]. This expansion is given in equation 6.

$$\dot{\boldsymbol{x}} = f(\boldsymbol{x}) + G(\boldsymbol{x})\boldsymbol{u} \text{ and } \boldsymbol{y} = h(\boldsymbol{x}) \tag{5}$$

$$\begin{aligned} \dot{\boldsymbol{x}} &\approx \dot{\boldsymbol{x}}_0 + \frac{\partial}{\partial \boldsymbol{x}}[\boldsymbol{f}(\boldsymbol{x}) + G(\boldsymbol{x})\boldsymbol{u}]_{\boldsymbol{u}_0,\boldsymbol{x}_0}(\boldsymbol{x} - \boldsymbol{x}_0) + \frac{\partial}{\partial \boldsymbol{u}}[\boldsymbol{f}(\boldsymbol{x}) + G(\boldsymbol{x})\boldsymbol{u}]_{\boldsymbol{u}_0,\boldsymbol{x}_0}(\boldsymbol{u} - \boldsymbol{u}_0) \\ &= \dot{\boldsymbol{x}}_0 + \frac{\partial}{\partial \boldsymbol{x}}[\boldsymbol{f}(\boldsymbol{x}) + G(\boldsymbol{x})\boldsymbol{u}]_{\boldsymbol{u}_0,\boldsymbol{x}_0}(\Delta \boldsymbol{x}) + G(\boldsymbol{x}_0)(\Delta \boldsymbol{u}) \end{aligned} \tag{6}$$

When the sample rate is high enough, the equation can be simplified to equation 7. For this time scale separation is applied, as it is assumed control surface deflections are faster than the aircraft dynamics [10].

$$\dot{\boldsymbol{x}} \approx \dot{\boldsymbol{x}}_0 + G(\boldsymbol{x}_0)\Delta \boldsymbol{u} \tag{7}$$

Inverting this equation and adding the previous control input gives the control law in equation 8.

$$\boldsymbol{u} = \boldsymbol{u}_0 + G^{-1}(\boldsymbol{x}_0)(\boldsymbol{v} - \dot{\boldsymbol{x}}_0) \tag{8}$$

The INDI control law that will be used is based on the rotational equations of motion, given in equation 9

$$\dot{\boldsymbol{\omega}} = \boldsymbol{I}^{-1}\boldsymbol{M} - \boldsymbol{I}^{-}1\,(\boldsymbol{\omega} \times \boldsymbol{I}\boldsymbol{\omega}) \tag{9}$$

Differentiating equation 9 with respect to the control surface deflections gives equation 10.

$$G(\mathbf{x}) = \frac{\rho V^2 Sc}{2} \boldsymbol{I}^{-1} \begin{bmatrix} C_{l_{\delta_{CS1L}}} & C_{l_{\delta_{CS1R}}} & C_{l_{\delta_{CS2L}}} & C_{l_{\delta_{CS2R}}} & C_{l_{\delta_{CS3}}} \\ C_{m_{\delta_{CS1L}}} & C_{m_{\delta_{CS1R}}} & C_{m_{\delta_{CS2L}}} & C_{m_{\delta_{CS2R}}} & C_{m_{\delta_{CS3}}} \\ C_{n_{\delta_{CS1L}}} & C_{n_{\delta_{CS1R}}} & C_{n_{\delta_{CS2L}}} & C_{n_{\delta_{CS2R}}} & C_{n_{\delta_{CS3}}} \end{bmatrix} \tag{10}$$

Which when filled into equation 8, gives the new control surface deflections, as shown in equation 11, in which $\boldsymbol{P}$ is the inverse of $\boldsymbol{B}$. However, there is a problem with this equation, as the control effectiveness matrix is not square, and thus can not be inverted. This problem will be solved with the control allocation, presented in the next section.

$$\mathbf{u} = \mathbf{u}_0 + \frac{2\boldsymbol{I}}{\rho V^2 * S * c} \boldsymbol{P}(\boldsymbol{\nu} - \dot{\boldsymbol{x}}_0) \tag{11}$$

2. Control Allocation

As the Flying-V has five different control surfaces, there are only three different moments that need to be controlled. This means that the control effectiveness matrix $\boldsymbol{B}$ has five columns and three rows, so the matrix cannot be inverted. This can be solved by using a pseudo-inverse, the choice of which impacts how the control surfaces are used. Furthermore, as the Flying-V has limited control authority, it is important that the control surfaces are used effectively. It is therefore preferable if the control allocation takes actuator limits into account. The maximum control deflections can be calculated using equation 12 [18].

$$\Delta \boldsymbol{u}_{max} = \min\left(\dot{\boldsymbol{u}}_{max} \frac{\omega_{act}}{2\zeta_{act}}, \boldsymbol{u}_{max} - \boldsymbol{u}\right) \text{ and } \Delta \boldsymbol{u}_{min} = \max\left(\dot{\boldsymbol{u}}_{min} \frac{\omega_{act}}{2\zeta_{act}}, \boldsymbol{u}_{min} - \boldsymbol{u}\right) \tag{12}$$

For control allocation, a cascading algorithm was chosen. The first step is to use a Moore-Penrose pseudo-inverse (as given in equation 13), to get the inverse of the control effectiveness matrix $\boldsymbol{B}$. Using the Moore-Penrose pseudo-inverse minimises the total control deflections [19].

$$\boldsymbol{P} = \boldsymbol{B}^T (\boldsymbol{B}\boldsymbol{B}^T)^{-1} \tag{13}$$

The required control deflections can be calculated with equation 14, in which $\boldsymbol{m}^*_{des}$ is defined in equation 15.

$$\boldsymbol{u} = \boldsymbol{P}\boldsymbol{m}^*_{des} \tag{14}$$

$$\boldsymbol{m}^*_{des} = \frac{2\boldsymbol{I}}{\rho V^2 Sc} (\boldsymbol{\nu} - \dot{\boldsymbol{x}}_0) \tag{15}$$

If none of the demanded control deflections are over the limits, calculated with equation 12, these control deflections are used as the output. If this is not the case, the following three scenarios will be checked, in this order:

1) If control surface 3 has reached its limit:
   - Control surface 3 will be set to either its limit or to the required yaw moment divided by $C_{l_{CS3}}$.
   - The column related to control surface 3, and the row related to the yaw moment is removed from the control effectiveness matrix $\boldsymbol{B}$. The desired yaw moment is removed from the $\boldsymbol{m}^*_{des}$.
   - The new $\boldsymbol{m}^*_{des}$ is calculated by subtracting the generated moment by Control surface 3 from $\boldsymbol{m}^*_{des}$.
2) Else, if either Control surface 2 left, or right (or both) have reached their limits:
   - Find which of these two control surfaces is the most over its limit, and calculate $a = u/u_{lim}$. Scale the other control surface with a, so that direction is preserved between these two control surfaces.
   - Calculate the new $\boldsymbol{m}^*_{des}$ by subtracting the generated moments from $\boldsymbol{m}^*_{des}$.
   - Remove the rows related to $\delta_{CS_{2_L}}$ and $\delta_{CS_{2_R}}$ from $\boldsymbol{B}$
3) Else, if either Control surface 1 left, or right (or both) have reached their limits:
   - Find which of these two control surfaces is the most over its limit, and calculate $a = u/u_{lim}$. Scale the other control surface with a, so that direction is preserved between these two control surfaces.
   - Calculate the new $\boldsymbol{m}^*_{des}$ by subtracting the generated moments from $\boldsymbol{m}^*_{des}$.
   - Remove the rows related to $\delta_{CS_{1_L}}$ and $\delta_{CS_{1_R}}$ from $\boldsymbol{B}$

If one of the inboard or outboard control surfaces is at its deflection limits, the other control surfaces are no longer scaled, to prevent the control surfaces from staying locked at their deflection limit. This means direction, the ratio between moments, is temporarily not guaranteed until the control surface is no longer at its limit.

After this, there are four cases:

1) $\boldsymbol{B}$ has more columns than rows: in this case, the Moore-Penrose pseudo-inverse is used to invert the $\boldsymbol{B}$.
2) $\boldsymbol{B}$ has the same amount of rows as columns: it can be inverted normally.
3) $\boldsymbol{B}$ has fewer columns than rows: The problem is now over-determined, and the result will not fully meet the desired moment. To minimize the error, the following pseudo-inverse is used [19]: $\boldsymbol{P} = \left(\boldsymbol{B}_{red}^T \boldsymbol{B}_{red}\right)^{-1} \boldsymbol{B}_{red}^T$
4) $\boldsymbol{B}$ is empty, meaning there are no control surfaces left to allocate. In this case, the control allocation does not completely meet the desired moment.

With the new inversed $\boldsymbol{B}$ matrix and $\boldsymbol{m}_{des}^*$ the other control surfaces can be allocated. If some control surfaces reach their limit, the algorithm starts again, until no surfaces are over the limit, or there are no control surfaces left to allocate.

B. Flight Control System

The overall control layout is based on the Flight control system proposed by Lombaerts [20], however, some changes were made. The angle of attack loop is removed, and the controller's load factor input is used straight into the reference model for longitudinal control, because the Flight Envelope Protection (FEP) law that is used limits the angle of attack by limiting the commanded load factor, making the angle of attack loop not necessary. The inner loop NDI controller is also replaced with an INDI control law. The way the FEP was implemented is also different, which will be elaborated on in section III.C. An overview of the Flight Control System can be found in Figure 4.

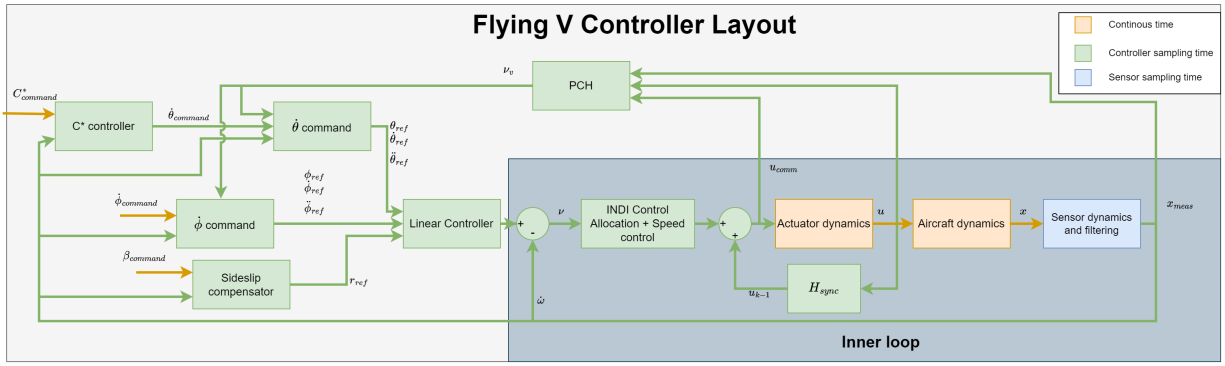

Fig. 4 Block diagram of the Flight Control System of the Flying-V

1. *C* controller*

For longitudinal control, a C^* controller is chosen. C^* control is based on the C^* criterion. The idea behind C^* control is that it is a mix of pitch rate and load factor control, where in lower speed regimes the pitch rate is dominant, whereas for higher speeds the load factor control is dominant [21]. C^* control is selected as Airbus also uses this control law in there Aircraft, for example, the A320 also uses C^* control [22]. This will increase the familiarity that pilots have when flying with the Flying-V for the first time [21]. It should be noted however that Airbus uses a combination of load factor and pitch rate feedback, that is not strictly C^* control [22].

The C^*-command is multiplied by $\frac{\cos(\theta)}{\cos(\phi)}$ to include turn compensation, as well as lower the commanded load factor at high pitch angles. [20]. After this, the pitch rate is subtracted from the command, to get a commanded load factor, which then is used to get a $\dot{\theta}_{command}$ for the pitch reference model. This is done with PI-control, combined with a feedforward path. The feedforward path is used to shape the aircraft's response to pilot inputs. An overview of the C^* controller can be seen in figure 5.

2. *Reference models*

The reference models for pitch and roll are largely identical. The difference between the reference models is that the roll protection is located in the roll reference model, which will be elaborated on in section III.C.

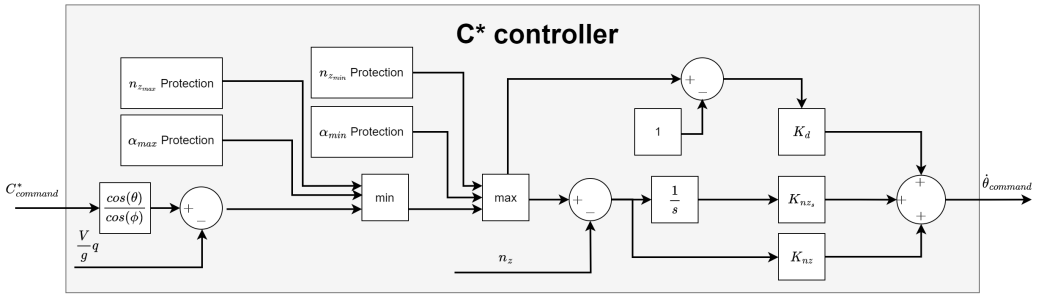

Fig. 5 Block diagram of the C^* controller

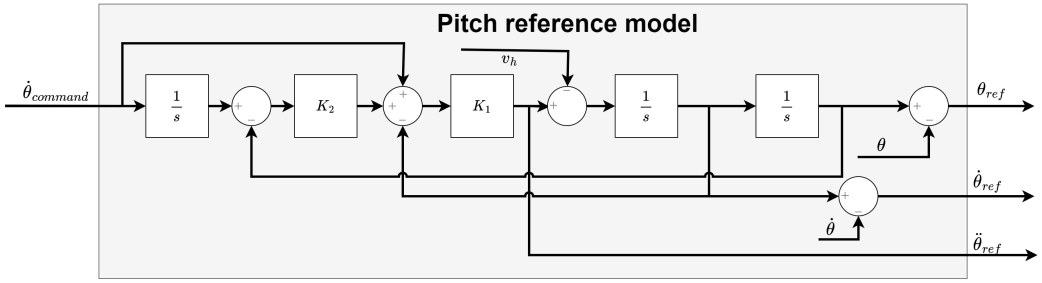

Fig. 6 Block diagram of the pitch reference model

Both reference models act as second-order filters. The relation between the gains and the natural frequency and damping ratio can be found in Equations 16.

$$K_1 = 2\zeta\omega \text{ and } K_2 = \frac{\omega}{2\zeta} \tag{16}$$

The roll reference model has as input a roll rate command from the pilot, and the reference model acts as a Rate Control Attitude Hold controller. A difference from the controller from Lombaerts [20] is that this control law does not switch to attitude control for roll angles above 30 degrees.

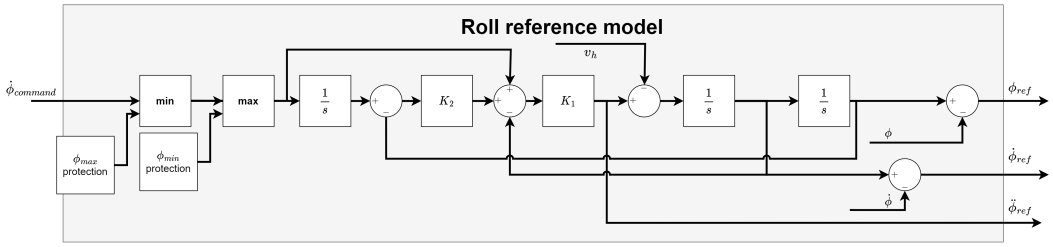

Fig. 7 Block diagram of the roll reference model

3. Sideslip Compensation

The block diagram for the sideslip compensator is given in figure 8. w is approximated with equation 17. This will take care of the control of the yaw channel, meaning that the FCS will have sideslip control, and not yaw rate control [20]. For this control law sideslip angle measurements are required.

$$w \approx V \sin(\alpha) \tag{17}$$

4. Linear controller

The linear controller converts the outputs of the reference models and sideslip compensator to the virtual control signal ν. It is a PI controller using the control laws given in equations 18, 19, and 20 which are obtained from Lombaerts[20].

$$\nu_p = \left(K_\phi + \frac{K_{\phi I}}{s}\right) \cdot \phi_{ref} + K_{\dot{\phi}} \cdot \dot{\phi}_{ref} + K_{\ddot{\phi}} \cdot \ddot{\phi}_{ref} \tag{18}$$

$$\nu_q = K_\theta \cdot \theta_{ref} + K_{\dot{\theta}} \cdot \dot{\theta}_{ref} + K_{\ddot{\theta}} \cdot \ddot{\theta}_{ref} \tag{19}$$

$$\nu_r = K_r \cdot r_{ref} \tag{20}$$

5. Pseudo Control Hedging

Pseudo Control Hedging (PCH) is a way to prevent actuator windup. PCH lowers the reference model signal, by calculating the difference between the demanded moment, and the estimated generated moment. The virtual control hedge can be calculated with equation 21, which are obtained from Grondman [17].

$$\boldsymbol{\nu}_h = G(\boldsymbol{x})(\boldsymbol{u}_{comm} - \boldsymbol{u}_{actual}) \tag{21}$$

The virtual control hedge will be subtracted from the reference models, as can be seen in figures 7 and 6. This means that difference in the yaw moment is not hedged. PCH will lower the commanded signals down to a level, which is obtainable by the control surface deflections.

6. Synchronisation Filter

In previous research, it was found that it is important for INDI that u_{k-1} is in sync with the angular acceleration measurements [23]. Time delays, originating from for example sensors, could make the difference in timing too large, degrading the performance of the FCS. To minimize this effect, a synchronisation filter is applied. This synchronisation filter consists of the same second-order filter that is applied to obtain the angular accelerations and a time delay. The time delay was set to be $2ms$ higher than the time delay of the angular rate sensor, to have room for unaccounted time delays

C. Flight Envelope Protection

The Flight Envelope Protection (FEP) consists of three different parts. Angle of Attack protection, load factor, and roll angle protection. The angle of attack and load factor protections limits the commanded load factor in the C^* controller, as is shown in figure 5 [24]. The roll angle protection does this with the commanded roll rate, as can be seen in 7.

1. Angle of Attack Protection

As the Flight Envelope Protection is implemented to ensure the Flying-V will stay in its flight envelope at all times, the angle of attack protection is very important, to prevent it from reaching pitch break-up. It is found that while the pitch

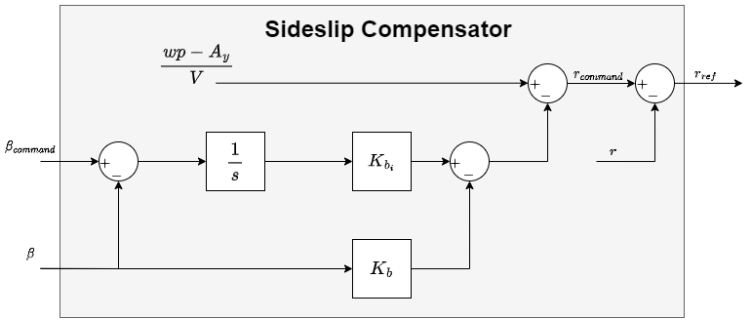

Fig. 8 Block diagram of the Sideslip compensator

break-up effect already starts at angles of attack above 20 degrees, it is important that the Flying-V does not reach an angle of attack higher than 34 degrees, as after this the aircraft can no longer recover itself, even with maximum control deflections. It should be kept in mind that this is in an optimal case, where the control surfaces could be deflected from maximum deflection to minimum, in practice, the maximal recoverable angle of attack will be lower. The maximum load factor, due to the angle of attack protection, $n_{z_{\alpha_{max}}}$ is calculated with equation 22, as well as the minimum $n_{z_{\alpha_{min}}}$ [24].

$$n_{z_{\alpha_{max}}} = n_z + K_{\alpha_{max}} (\alpha_{max} - \alpha) \quad \text{and} \quad n_{z_{\alpha_{min}}} = n_z + K_{\alpha_{min}} (\alpha_{min} - \alpha) \tag{22}$$

The maximum angle of attack protection only becomes active for angles of attack higher than 15 degrees, and the minimum for angles of attack below 0 degrees, this is done to make sure the protection does not limit the Flying-V's maneuverability in normal flight. The signals are respectively 2.5 and -1 when the protections are inactive.

2. Load factor protection

The maximum load factor can be calculated using equation 23 [20]. In this equation $C_{L_{max}}$ is set to the C_L at an angle of attack of 25 degrees, and $\Delta C_{L_{max}}$ is set to 0.01.

$$n_{z_{max}} = \max\left(1, \min\left(2.5, 1 + \frac{(C_{L_{max}} - \Delta C_{L_{max}})\overline{q}S}{W} \cos(\phi) - n_y \sin(\phi) - \cos(\gamma) + \frac{T}{W} \sin(\alpha) \cos(\phi)\right)\right) \tag{23}$$

The minimum load factor, $n_{z_{min}}$ is equal to -1 [20].

3. Roll angle protection

The maximum roll angle (in degrees) can be calculated with equation 24 [20]. This is then transformed to a maximum and minimum roll rate signal with equation 25.

$$\phi_{max} = \min\left(66, \arccos\left(\frac{mg \cos(\gamma)}{T \sin\alpha + (C_{L_{max}} - \Delta C_{L_{max}})\overline{q}S}\right)\right) \tag{24}$$

$$\dot{\phi}_{max} = K_{\phi_{protec}}(\phi_{max} - \phi) \text{ and } \dot{\phi}_{min} = K_{\phi_{protec}}(-\phi_{max} - \phi) \tag{25}$$

The roll angle protection is only active when the roll angle is within two degrees of the limit, so the protection does not limit the maneuverability in normal flight.

IV. Tuning and Performance evaluation

In this section it is presented how the performance of the FCS will be evaluated. First, the tuning of the FCS parameters is explained. After this, additional performance evalutation metrics are presented. Next to that it is given how the effects of sampling time and aerodynamic uncertainties will be evaluated. Finally the method of testing the FEP laws is presented.

A. Tuning

For tuning of the gains of the control laws, multi-objective optimisation is used. The longitudinal design parameters (C^*-controller, pitch reference model, and the ν_q control law) is tuned separately from the lateral parameters. This can be done as they do not influence the scoring of the other part.

The tuning is done using an optimization algorithm, that for the first run will generate a list of 200 numbers for the gains, following a normal distribution. For these gains, a score is calculated, using the objectives given in the next section. The best scoring combinations of gains then is used to generate the next list of gains. The tuning algorithm stops when the score does not improve for two runs in a row.

This method of tuning the gains does converge on a minimum score. However as it is a problem with many local minima, this does not mean the gains that are found is the combination of gains that are the best solution for the problem. It is therefore important to use multiple different initial guesses for tuning.

1. Tuning Objectives

The longitudinal tuning objectives can be found in table 2. The lateral tuning objectives are given in table 3. The constraint objectives are based on requirements from MIL-STD-1797A [25], and will have a score of 0 when in level 1 flying qualities, a score of 100 plus extra for the distance from level 1 when in level 2, and a score of 1000 plus extra for the distance from level 2 when in level 3 or worse. The distance is the difference in the value of the two levels, and is multiplied respectively with 50 and 500.

Table 2 Longitudinal tuning objectives

Description	Type	Min level 2	Min Level 1	Max Level 1	Max Level 2
Linear Analysis					
Gain Margin ν_q $[dB]$	Constraint	0	6	-	-
Phase Margin ν_q $[deg]$	Constraint	0	45	-	-
ω_{sp} $[rad/s]$	Constraint	0.6	1	-	-
ζ_{sp} $[-]$	Constraint	0.25	0.35	1.3	2
CAP $[g^{-1}s^{-2}]$	Constraint	0.038	0.085	3.6	10
ω_{BW} $[rad/s]$	Constraint	1	3	-	-
τ_p $[s]$	Constraint	-	0	0.1	-
$score_{LOES}$ $[-]$	Constraint	-	-	15	100
ω_{CO} $[rad/s]$	Minimize	-	-	-	-
Simulation with C^*_{comm} step input of 1.8 at t = 1s. T_{sim} = 20s					
max(δ_{CS}) $[deg]$	Minimize	-	-	-	-
$\delta_{CS_{activity}}$ $[deg/s]$	Minimize	-	-	-	-
Settling Time C^* $[s]$	Minimize	-	-	-	-
Overshoot C^* $[-]$	Minimize	-	-	-	-

For the simulations, the actuator activity will be determined with equation 26, and will be the average of all the five control surfaces. The settling time is the time from the start of the step input until the signal is within 1% of the commanded signal. Overshoot (OS) will be calculated with equation 26. These extra parameters are used to minimise control surface activity.

$$\delta_{CS_{activity}} = \frac{\int_0^T |\dot{\delta}_{CS}|dt}{T} \quad \text{and} \quad OS = max\left(\frac{y_{actual} - y_{command}}{y_{command}}\right) \tag{26}$$

2. Gain and Phase Margins

The gain and phase margins are determined by opening the loop after the summation point after the Linear Controller in figure 4. The objective for the crossover frequency is to be minimised, however, a too low crossover frequency can reduce the disturbance rejection capabilities of the FCS [26], to ensure enough disturbance rejection capabilities, a minimum crossover frequency of 5 rad/s was set.

3. Low Order Equivalent System

To obtain the short period parameters, as well as the Control Anticipation Parameter, a Low Order Equivalent System (LOES) is fitted on the pitch rate transfer function. To get the LOES fit, the pitch rate response and load factor response should be fit simultaneously. The reduced order model of the pitch rate can be found in equation 27. [25]

$$\frac{q(s)}{\delta_{es}(s)} = \frac{K_q s\left(s + \frac{1}{T_{\theta_1}}\right)\left(s + \frac{1}{T_{\theta_2}}\right)e^{-\tau_e s}}{\left(s^2 + 2\zeta_{sp}\omega_{sp}s + \omega_{sp}^2\right)\left(s^2 + 2\zeta_{ph}\omega_{ph}s + \omega_{ph}^2\right)} \tag{27}$$

If the natural frequency of the phugoid and short-period is separated sufficiently, with at least a factor 10, the two modes can be looked at separately [25]. This reduces the model to equation 28 [27].

Table 3 Lateral tuning objectives

Description	Type	Min level 2	Min Level 1	Max Level 1	Max Level 2
Linear Analysis					
Gain Margin ν_p $[dB]$	Constraint	0	6	-	-
Phase Margin ν_p $[deg]$	Constraint	0	45	-	-
Gain Margin ν_r $[dB]$	Constraint	0	6	-	-
Phase Margin ν_r $[deg]$	Constraint	0	45	-	-
$1/T_s$ $[s^-1]$	Constraint	-0.087	-0.058	-	-
T_r $[s]$	Constraint	0	-	1	1.4
ω_{dr} $[rad/s]$	Constraint	0.4	0.5	-	-
ζ_{dr} $[-]$	Constraint	0.02	0.08	-	-
$\omega_{dr}\zeta_{dr}$ $[rad/s]$	Constraint	0.05	0.015	-	-
$score_{LOES}$ $[-]$	Constraint	-	-	15	100
ω_{CO_p} $[rad/s]$	Minimize	-	5	-	-
ω_{CO_r} $[rad/s]$	Minimize	-	5	-	-
Simulation with $\dot{\phi}_{comm}$ block input of 3 deg between t = 1s and t = 14s. T_{sim} = 18s					
max(δ_{CS}) $[deg]$	Minimize	-	-	-	-
$\delta_{CS_{activity}}$ $[deg/s]$	Minimize	-	-	-	-
Settling Time $\dot{\phi}$ $[s]$	Minimize	-	-	-	-
Simulation with Wind step w_{wind} = 16 m/s at t = 1s. T_{sim} = 15s					
$\delta_{CS_{activity}}$ $[deg/s]$	Minimize	-	-	-	-

$$\frac{q(s)}{\delta_{es}(s)} = \frac{K_q\left(s+\frac{1}{T_{\theta_2}}\right)e^{-\tau_e s}}{\left(s^2+2\zeta_{sp}\omega_{sp}s+\omega_{sp}^2\right)} \quad \text{and} \quad \frac{n_z'(s)}{\delta_{es}(s)} = \frac{K_n e^{-\tau_n s}}{\left(s^2+2\zeta_{sp}\omega_{sp}s+\omega_{sp}^2\right)} \tag{28}$$

The reduced load factor model that should be fitted simultaneously, in accordance with MIL-STD-1797A [25] is given in the same equation. n_z' is the normal acceleration at the instantaneous center of rotation.

The LOES is fitted on the linearized High Order System (HOS), by matching its frequency response between 0.1 and 10 [rad/s] [25]. MIL-STD-1797A [25] however mentions that there is insufficient data on how to best score the matching of the LOES and HOS, but suggests using equation 29, in which G is the gain in dB and ϕ the phase in degrees over 20 frequency points evenly spaced on a logarithmic scale, with K having a value around 0.02 [28].

$$M = \Sigma(G_{HOS} - G_{LOES})^2 + K\Sigma(\phi_{HOS} - \phi_{LOES})^2 \tag{29}$$

The disadvantage of this method is that it weighs the error at every frequency point the same, where it was found that the match at frequencies around 1-4 rad/s was more important than at other frequencies. Therefore the Maximum Unnoticeable Added Dynamics envelopes were developed. These envelopes can be approximated with the transfer functions in table 4.

Table 4 MUAD envelope transfer functions

	Upper bound	Lower bound
Gain	$\frac{3.16s^2+31.61s+22.79}{s^2+27.14+1.84}$	$\frac{9.55\cdot10^{-2}s^2+9.92s+2.15}{s^2+11.60s+4.95}$
Phase	$\frac{68.89s^2+1100.12s-275.22}{s^2+39.94+9.99}$	$\frac{475.32s^2+184100s+29456.1}{s^2+11.66s+3.89\cdot10^{-2}}e^{-0.0072s}$

For this research, a weighting factor is applied which is the inverse of the maximum allowable gain or phase mismatch, according to the MUAD envelope. It should be noted that the envelopes are not symmetric so that the weight

can be different depending if the LOES has a higher or lower value at the same frequency than the HOS [29]. The score is calculated with equation 30.

$$M = \Sigma((G_{HOS} - G_{LOES}) * w_G) + \Sigma((\phi_{HOS} - \phi_{LOES}) * w_\phi) \tag{30}$$

After the low order model is fitted, the short period frequency and damping ratio can be found. The Control Anticipation Parameter (CAP) can be found with equation 31.

$$CAP = \frac{\dot{q}}{n_{z_{ss}}} = \frac{\omega_{sp}^2}{n_\alpha} \quad \text{and} \quad n_\alpha = \frac{V}{gT_{\theta_2}} \tag{31}$$

For the lateral tuning, there is another low-order equivalent system required. The LOES for roll angle is given in equation 32, which should be fitted together with the sideslip LOES given in the same equation [25]. The method of fitting the LOES to the HOS is the same as for the longitudinal case.

$$\frac{\phi}{\delta_{as}} = \frac{K_\phi \left(s^2 + 2\zeta_\phi \omega_\phi s + \omega_\phi^2\right) e^{-\tau_{ep} s}}{\left(1 + \frac{1}{T_s}\right)\left(1 + \frac{1}{T_r}\right)\left(s^2 + 2\zeta_d \omega_d s + \omega_d^2\right)} \quad \text{and} \quad \frac{\beta}{\delta_{rp}} = \frac{\left(A_3 s^3 + A_2 s^2 + A_1 s + A_0\right) e^{-\tau_{e\beta} s}}{\left(1 + \frac{1}{T_s}\right)\left(1 + \frac{1}{T_r}\right)\left(s^2 + 2\zeta_d \omega_d s + \omega_d^2\right)} \tag{32}$$

The spiral mode is allowed to be unstable, as long as the time to double the amplitude T_2 is larger than 20 s. The relation between the time constant and doubling time is given in equation 33 [28].

$$T_2 = -T_s \ln(2) \tag{33}$$

4. Attitude Bandwidth

Bandwidth is defined as the highest frequency with either a phase margin of 45 degrees, or a gain margin of 6 dB. It is found by finding the frequency $\omega_{BW_{phase}}$ where the phase equals -135 deg. Then find the frequency $\omega_{BW_{gain}}$ where the gain is 6 dB higher than the gain where the phase is -180 deg. The lower frequency of $\omega_{BW_{phase}}$ and $\omega_{BW_{gain}}$ is the bandwidth [25].

As not only the bandwidth frequency itself influence how the pilot experiences the aircraft, but also the phase roll-of, the equivalent time delay parameter τ_p needs to be evaluated. τ_p can be calculated with equation 34, in which ω_{180} is the frequency at phase = -180 deg, and $\phi_{2_{\omega_{180}}}$ is the phase at ω_{180} [25].

$$\tau_p = -\frac{(\phi_{2_{\omega_{180}}} + 180^\circ)}{57.3 \cdot 2 \cdot \omega_{180}} \tag{34}$$

B. Additional evaluation criteria

The first measurement of the performance of the controller is the ability to be tuned to level 1 flying qualities for set objectives. However, there are also other handling requirements, that are not used for tuning.

1. Extra Handling qualities

The evaluated extra requirements are Pitch attitude dropback, Gibson phase rate, Flight-path angle bandwidth, and the equivalent time delays of the low order equivalent systems.

The pitch attitude dropback was developed to evaluate highly augmented control systems by Gibson [30]. This criterion can be used to predict the possibility of Pilot Induced Oscillations. If this criterion is combined with the bandwidth and equivalent phase delay, the criterion is a good predictor for PIO [31]. The criterion can be evaluated by time-domain analysis from a block longitudinal stick input.

The Gibson phase rate criterion looks at the phase roll of around the crossover frequency, making it comparable with the equivalent time delay parameter.

The flight path bandwidth requirement is a requirement to make sure that the relation between the flight path and pitch attitude response appears reasonable to the pilot. The flight path bandwidth ω_{BW_γ} is defined as the frequency where the phase of the flight path lags the stick input by 135 degrees [31].

To ensure that the perceived time delay caused by the sensors and filters is not too large, which could degrade the tracking capabilities of the pilot, there are limits on the maximum equivalent time delay of the pitch rate and roll LOES model. [25]. To be within level 1, the equivalent time delay should be no more than 0.1 s [25].

2. Sampling time and Aerodynamic uncertainties

As there is not much aerodynamic data for the Flying-V available yet, there are quite some uncertainties for this data. Especially as the data that is used for this research is based on a combination of two data-sets, and is linearly interpolated between two Mach numbers.

To evaluate the effect of aerodynamic uncertainties, 100 simulations will be run, with all the aerodynamic parameters being varied with a normal distribution with a standard deviation of 20% of the parameter. The aerodynamic data used for the INDI control law and pseudo-control hedging will not change, introducing a difference in what the control law uses as aerodynamic data, and what the actual data is.

In reality, when the Flying-V is getting closer to being a commercial aircraft, more accurate aerodynamic data will be available, but there will still be a difference in the actual aerodynamic properties.

The simulation will be of 25 s, and have a step roll rate input of 5 $[deg/s]$ between 5 and 15 s. As the C^* input gets multiplied with the roll angle, this manoeuvre will also contain a changing longitudinal input. The first parameter that will be evaluated is the tracking RMS error, for the C^* and roll rate tracking, which are calculated with equation 35

$$\epsilon_{RMS} = \sqrt{\frac{1}{n}\Sigma(y_{actual} - y_{command})^2} \tag{35}$$

The other parameter that is evaluated is the control surface activity, which is calculated with equation 26.

The effect of sampling time will be analysed with the same method, with 100 simulations varying the sampling frequency from 1000 Hz down to 10 Hz, the tuning will be done for a sampling frequency of 100 Hz.

3. FEP testing

To test the flight envelope protection, the following requirements for the FEP were set:

- The FEP laws should not engage when flying well within the normal flight envelope [32]
- The normal acceleration n_z should not go out the limit of -1g ≤ Nz ≤ 2.5g [33]
- The angle of attack should not go over 30 degrees

For the evaluation, two different simulations will be done, as they were found to be the most challenging for the flight envelope protection laws. The first simulation will have a step C^* input of 2, with thrust set to 0. The second simulation will have the same C^* input, but for t = 5s until t = 15s also have a $\dot{\phi}_{comm}$ of 5 degrees. Both simulations will run for 250 seconds. The simulations will be done starting from a height of 13 km and 1 km.

V. Results and discussion

In this section the results of this research will be presented and discussed. First, the results from tuning the FCS will be given in cruise and approach conditions, with and without the contribution of sensor dynamics and discretization effects. After this, in section V.B the other handling qualities will be evaluated for the Flying-V with the sensor dynamics. The effects of different sampling frequencies is evaluated in section V.C. Then the effects of aerodynamic uncertainties are presented in section V.D and finally the FEP laws are evaluated in section V.E.

A. Tuning results

An overview of the results for tuning in cruise conditions can be seen in figure 9. The complete longitudinal tuning results are given in table 5a, and in table 5b the complete lateral tuning results.

The handling qualities of the model without sensor dynamics and without the discretization effects are all well within level 1. The gain and phase margins are also larger than required. It should be noted that the gain margin for pitch is negative, indicating that the open-loop is unstable, but the closed-loop is not.

When adding the sensor dynamics and making the controller discrete, the gain and phase margins become smaller, as expected. Where all the handling quality requirements are still within level 1, the gain and phase margin requirements are no longer met. Therefore a third model was made, with an angular rate sensor with less time delay. For the new sensors, the time delay for the angular rates is changed to 0.04 s, with a filter time constant of 0.03. These values for the sensor parameters will be used for the next results, as well as the tuning for the adjusted sensors. It should be noted that when the sampling frequency of the angular rate sensor was set to 100 Hz, and the time delay to 0.05 s, the FCS could also be tuned to be within level 1 handling requirements, with enough gain and phase margins. For higher time delays a compromise between enough bandwidth and phase margin could no longer be found.

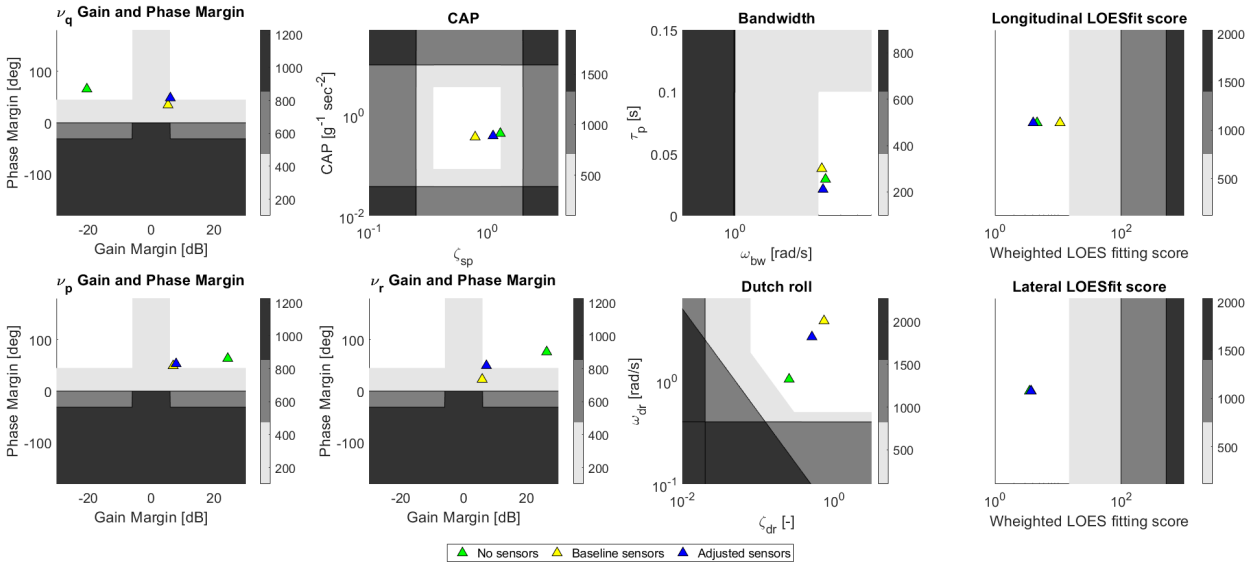

Fig. 9 Tuning scores for tuning in cruise conditions

Table 5 Tuning results. Green being within level 1, and yellow being within level 2 Handling Qualities

(a) Longitudinal tuning results for cruise conditions.

Description	No sensors	Adjusted sensors	Baseline sensors
Linear Analysis			
GM ν_q $[dB]$	20.37	6.08	5.35
PM ν_q $[deg]$	65.34	48.06	34.5
ω_{sp} $[rad/s]$	1.81	1.82	2.18
ζ_{sp} $[-]$	1.29	1.12	0.79
CAP $[g^{-1}s^{-2}]$	0.433	0.388	0.368
ω_{BW} $[rad/s]$	3.27	3.17	3.12
τ_p $[s]$	0.029	0.021	0.038
$score_{LOES}$ $[-]$	4.67	4.05	10.79
ω_{CO} $[rad/s]$	34.7	7.72	6.19
Simulation with C^*_{comm} step input of 1.8 at t = 1s. T_{sim} = 20s			
max(δ_{CS}) $[deg]$	10.97	11.21	11.20
$\delta_{CS_{activity}}$ $[deg/s]$	0.17	0.69	0.77
ST C^* $[s]$	3.89	2.72	4.48
OSC* $[-]$	0.08	0.08	0.13

(b) Lateral tuning results for cruise conditions

Description	No sensors	Adjusted sensors	Baseline sensors
Linear Analysis			
GM ν_p $[dB]$	24.28	7.91	6.97
PM ν_p $[deg]$	63.16	52.95	48.98
GM ν_r $[dB]$	26.29	7.19	5.85
PM ν_r $[deg]$	75.95	49.28	22.82
$1/T_s$ $[s^{-1}]$	0.074	0.065	0.07
T_r $[s]$	0.513	0.604	0.52
ω_{dr} $[rad/s]$	1.036	2.66	3.81
ζ_{dr} $[-]$	0.26	0.52	0.74
$\omega_{dr}\zeta_{dr}$ $[rad/s]$	0.27	1.37	2.83
$score_{LOES}$ $[-]$	3.54	3.74	3.77
ω_{CO_p} $[rad/s]$	36.29	6.69	5.10
ω_{CO_r} $[rad/s]$	29.75	5.96	5.56
Simulation with $\dot{\phi}_{comm}$ block input of 3 deg between t = 1s and t = 14s. T_{sim} = 18s			
max(δ_{CS}) $[deg]$	6.04	7.74	4.1
$\delta_{CS_{activity}}$ $[deg/s]$	0.75	1.78	1.29
ST $\dot{\phi}$ $[s]$	5.27	4.42	5.53
Simulation with Wind step v_{wind} = 16 m/s at t = 1s. T_{sim} = 15s			
$\delta CS_{activity}$ $[deg/s]$	1.89	3.07	6.91

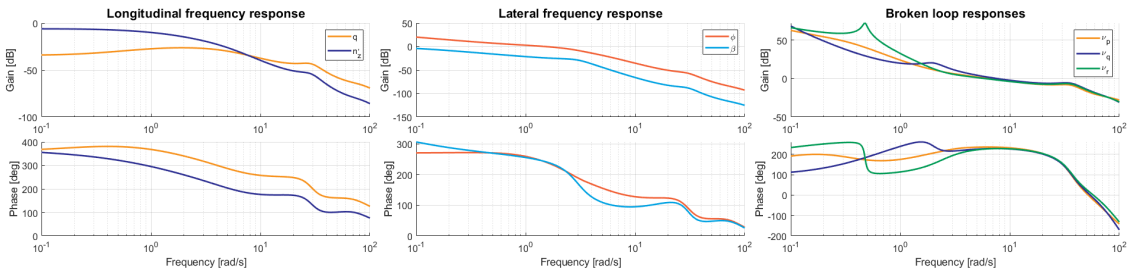

Fig. 10 Frequency responses in cruise condition with the adjusted sensor model

In figure 10 the frequency responses for the adjusted sensors model and tuning is given, as well as the broken-loop frequency responses. The two bumps present around 20 and 40 rad/s are caused by the sensor and actuator dynamics.

In figure 11 the response to a C^* block input is given for the three models, with the best found tuning for each case. There are two main differences, the first one is that the model with the baseline sensors shows multiple oscillations in the C^* response, whereas the other two models do not show this behavior. This is in accordance with the fact that this case has a lower phase margin than the two other models. The other main difference is the deflection of the rudder. The rudder in the model without sensors does not move, which is as expected, as the maneuver is purely longitudinal. However, the rudder oscillates a lot in the other two models. This is caused by the noise from the sideslip sensor. To improve on this behavior, the time constant of the sideslip filter was changed to 0.1 for the adjusted sensors case. This reduces the chatter of the rudder marginally, but the behavior is still apparent.

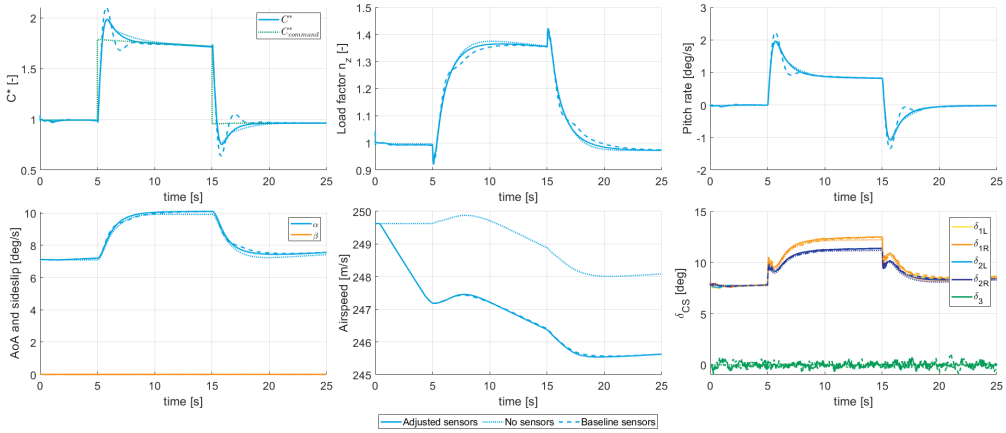

Fig. 11 C^* step response in cruise conditions

The time response to a $\dot{\phi}_{comm}$ block input is presented in figure 12. Here the model with the adjusted sensors response has more overshoot, but also a smaller settling time, indicating that the tuning for this model was more aggressive. This is also shown in the control surface deflections, which are larger for the adjusted sensor model. This difference is however not inherent on the model, but is a different solution found by the tuning algorithm. The chatter of the rudder is also present here for the baseline and adjusted sensors.

After the tuning was done for cruise conditions, and sensor parameters were determined for which level 1 handling qualities could be obtained, the FCS in approach conditions was evaluated. The results for this can be found in figure 13. As can be seen in this figure, retuning was required, as the cruise condition tuning no longer met the bandwidth requirement, as well as the LOES had a large mismatch. After retuning all handling qualities are again in level 1. Furthermore, after the retuning, the new handling quality parameters are close to the values of the cruise tuning, in cruise conditions. This indicates that the aircraft would react in a comparable way in this condition, as in cruise conditions, making the aircraft more predictable, and easier to fly.

B. Other Handling Qualities

An overview of the handling qualities parameters in cruise conditions is given in table 6.

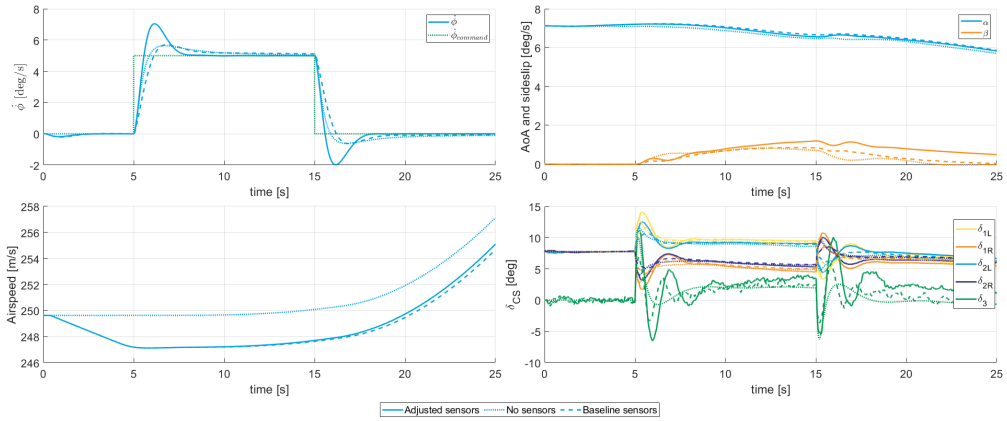

Fig. 12 Roll rate step input response in cruise conditions

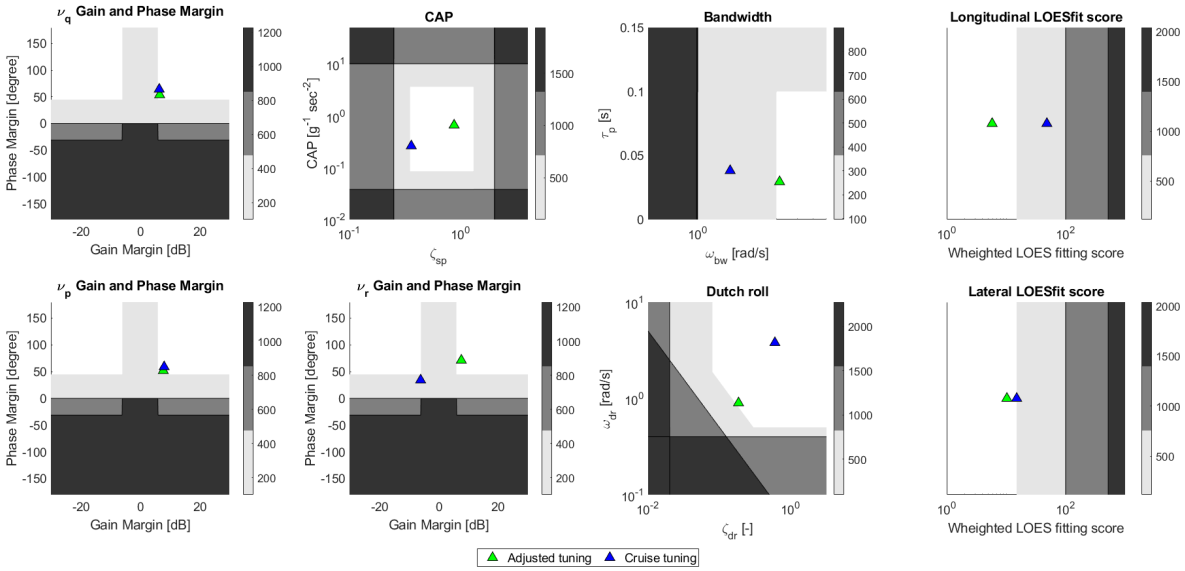

Fig. 13 Tuning scores for tuning in approach conditions

As can be seen in figure 14, the pitch attitude dropback is in the acceptable region. Next to that, it can also be seen that the phase rate criterion is also met, which was as expected, as the bandwidth requirement was also met. The phase rate is even in the optimum design region.

The flight path bandwidth is on the edge of the requirement, as shown in figure 14, but is in the level 1 area. All the time delays are lower than 0.1 s, except for the sideslip time delay. However, this is not a problem, as the 0.1s requirement is only applicable for the other time delays, where for sideslip higher time delays are acceptable [25].

C. Influence of sampling time

In figure 15 the RMS tracking error and control surface activity for varying sampling frequency is given. The trend in the tracking error and controller activity that can be observed is that with a longer sampling time, the error gets larger. This is as expected. However, for the range that is looked at, the error does not increase much, and there is a lot of variance. The chosen sampling frequency of 100 Hz that is used previously is deemed sufficient, as the error does not seem to decrease much with higher sampling frequencies.

In figure 16 the time traces for the varying sampling times are given. Where it also can be observed that for the range between 1000 and 10 Hz, the FCS is capable of tracking the roll rate reference signal, without much difference in tracking error, or control surface deflections. When increasing the sampling time above 0.1 s, the system becomes

Table 6 Extra Handling qualities parameters in cruise condition

Parameter	Value	Parameter	Value
$\frac{q_{peak}}{q_{ss}}$ [-]	1.9255	τ_{eq} [s]	0.057
$\frac{\Delta\theta_{peak}}{q_{ss}}$	1.33	τ_n [s]	0.047
Average phase rate [deg/Hz]	18.53	τ_{ep} [s]	0.079
ω_{-180} [deg]	1.079	$\tau_{e\beta}$ [s]	0.156
ω_{BW_γ} [rad/s]	0.61		

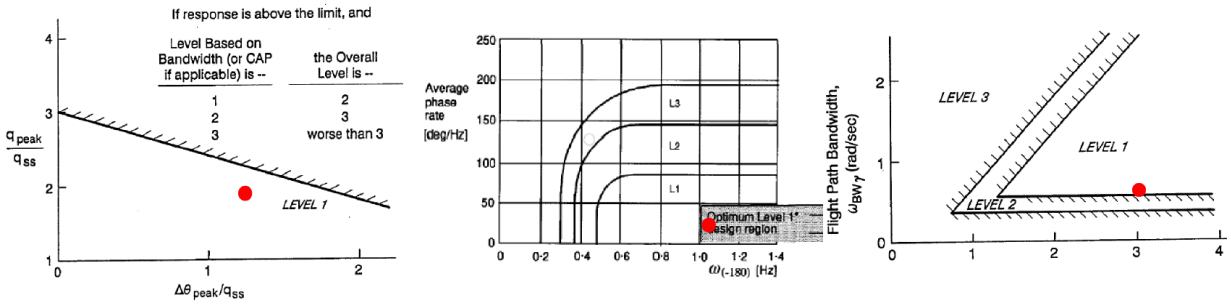

Fig. 14 Pitch attitude dropback, phase rate and Flight path bandwidth results in cruise, adapted from Mitchell [31] and Gibson [30]

unstable. As a sample rate of 100 Hz for a control system is easily obtainable, it can be concluded that the sampling rate will not be a problem for the FCS, as the performance, as well as the gain and phase margins for a sampling rate of 100 Hz are all within the requirements that were set.

D. Aerodynamic uncertainties

The variance of the tracking error and control surface activity, with varying aerodynamic uncertainties is given in figure 17. For the C^* and roll rate tracking error, there is little spread. With the maximum difference in C^* tracking error being 25 %, and also in roll rate tracking the difference between the highest and lowest value is roughly two thirds. This indicates that the FCS is robust in roll and C^* tracking for varying model parameters.

The variance of the inboard and outboard control surface activity is also small, and is caused by the variance in control surface effectiveness. The spread in rudder activity is however larger.

To explain the larger in variance, the time responses are plotted in figure 18. There you can see large oscillations in rudder deflection, as well as a large initial deflection, with for certain cases even reaching the deflection limit. As the

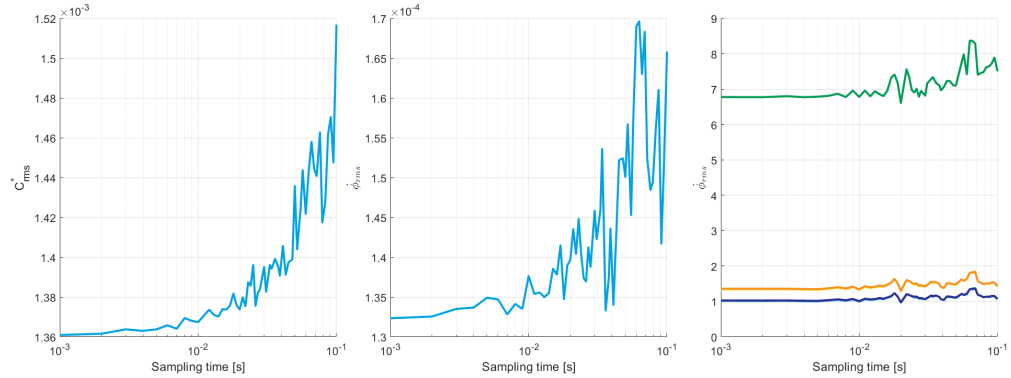

Fig. 15 Tracking error and controller activity for varying sampling times

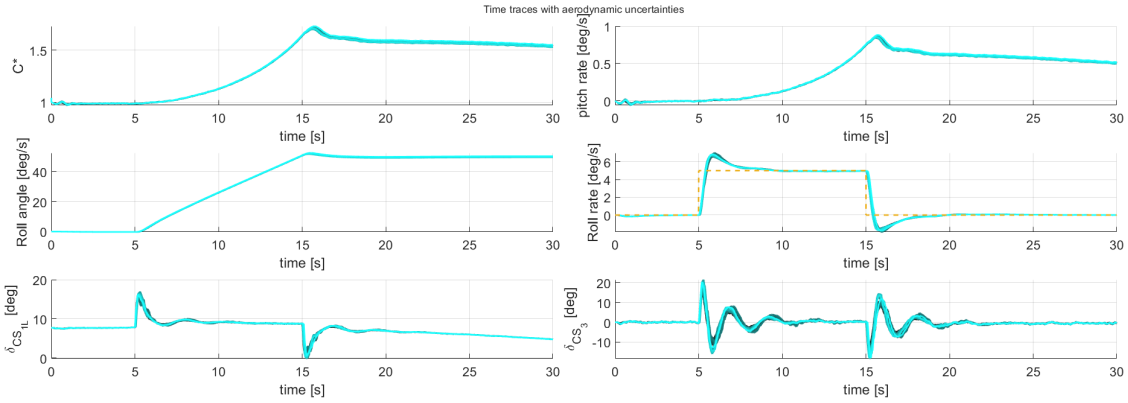

Fig. 16 Response to roll rate step, with varying sampling time, where lighter color = higher sampling time

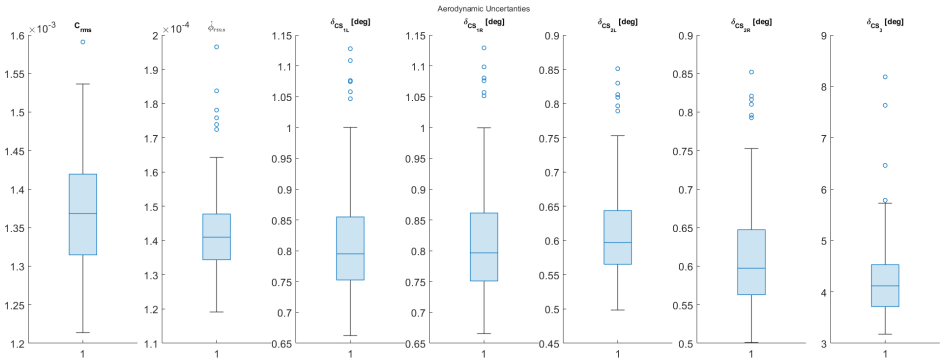

Fig. 17 Boxplots showing the variance in tracking error and control surface activity, with varying aerodynamic uncertainty

control authority of the rudder is already low in nominal conditions, the extra oscillations can be explained by the fact that the simulations with extra rudder activity, are the simulations where the rudder effectiveness is reduced. In the figure, it can also be seen that all simulations reach a trim position within 5 seconds and that there is almost no variation in roll rate and C^* tracking after the first five seconds. This shows that the FCS is robust for aerodynamic uncertainties, but if the control authority of the rudder is found to be lower than expected, this could be problematic.

E. Flight Envelope Protection

To improve the performance of the Flight Envelope Protection, first gain scheduling was implemented, as the airspeed during the manoeuvres changes a lot. The gain scheduling is dependent on the airspeed and is linearly interpolated between the cruise condition tuning, and tuning done at a airspeed of 100 m/s at an altitude of 1 km. For the lateral gains, a third point was added tuning at 70 m/s at an altitude of 1 km.

After tuning the Flight Envelope Protection control law gains, it was found that the angle of attack protection gain should be made air density dependant, to ensure that for all altitudes, the FEP is able to prevent the Flying-V reaching angle of attacks higher than 30 degrees. The FEP parameters that were used are given in table 7. The gain for minimum and maximum angle of attack was set to the same value.

Table 7 Flight envelope protection parameters

Parameter	Value for $\rho = 1.225$	Value for $\rho = 0.26$
$\alpha_{max}[deg]$	22	24
K_α	0.025	0.01
$K_{\phi_{protec}}$	0.3	0.3

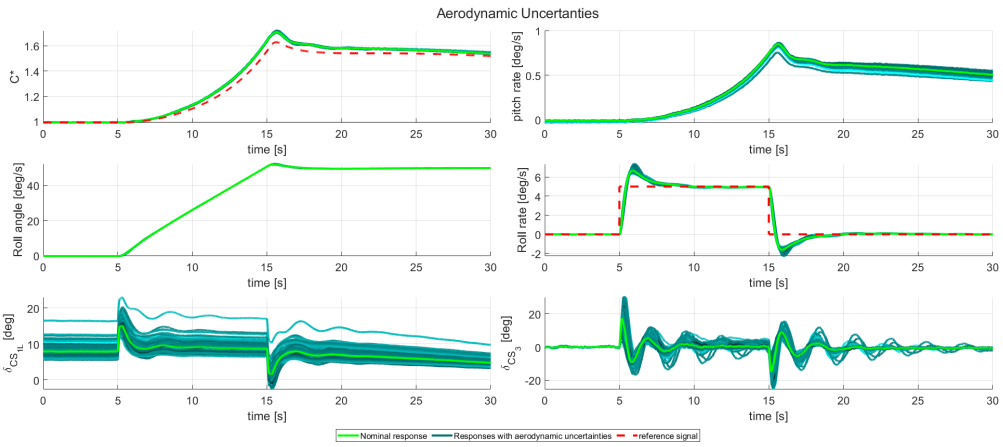

Fig. 18 Response to roll rate step, with varying aerodynamic uncertainty, where lighter color = more uncertainty

In figure 19 the results are given from the simulation starting at 13 km altitude, with only the C^* input. It can be seen that around t = 35s the angle of attack protection becomes active, after the angle of attack is above 15 degrees. However, the protection only starts limiting the load factor after t = 45 s. There is then an overshoot of just under 3 degrees, but keeping the angle of attack well below the maximum of 30 degrees. The angle of attack goes down to 20 degrees, while in the meantime the pitch angle goes down from just above 45 degrees to around -5 degrees. After t = 100s, the angle of attack converges at α_{max}. It should further be noticed that the oscillations of the rudder around t = 50s and t = 120s increases. This coincides with the moments the airspeed of the aircraft is the lowest at around 100 m/s. As the tuning at 100 m/s was done at an altitude of 1 km, and it is now at an altitude of 13 km, there is less dynamic pressure, than what the controller was tuned for.

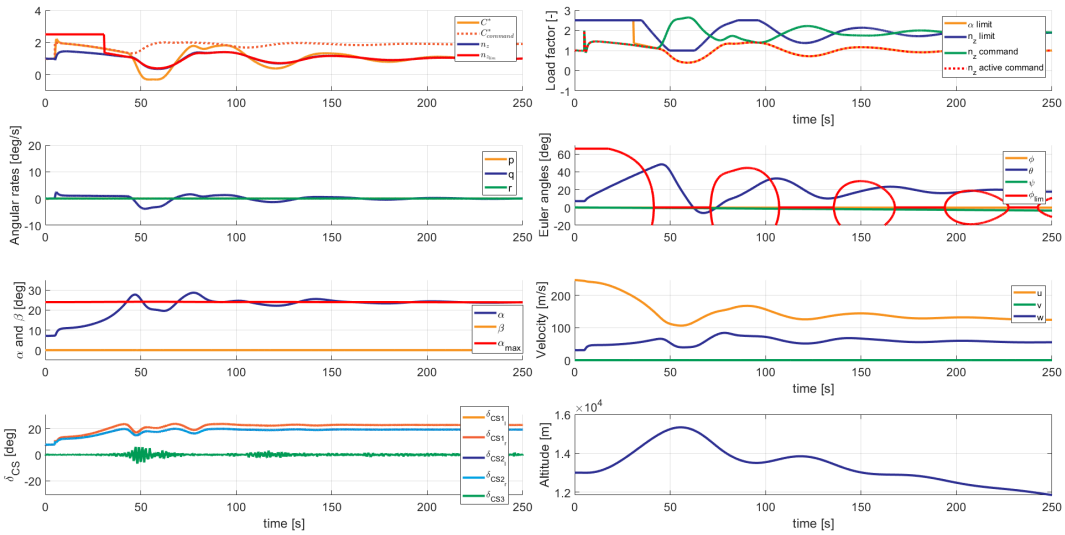

Fig. 19 Flight Envelope Protection starting from cruise height

In figure 20 the simulation starting from cruise conditions, with a roll rate input is given. When looking at the longitudinal protection, it is nearly identical to the values in figure 19. This is a good sign, as this means that the added roll angle, and roll protection is not degrading the performance of the longitudinal flight envelope protection. After t = 55s, the max roll angle becomes smaller than the current roll angle, and the protection starts to demand a negative roll angle. The roll angle becomes zero around t = 70 s. During this period, the rudder is oscillating from maximum to minimum deflections, this is because of the low dynamic pressure, combined with the tuning that was not done for this point.

The last simulation for the flight envelope protection is given in figure 21. This is the simulation that starts at an

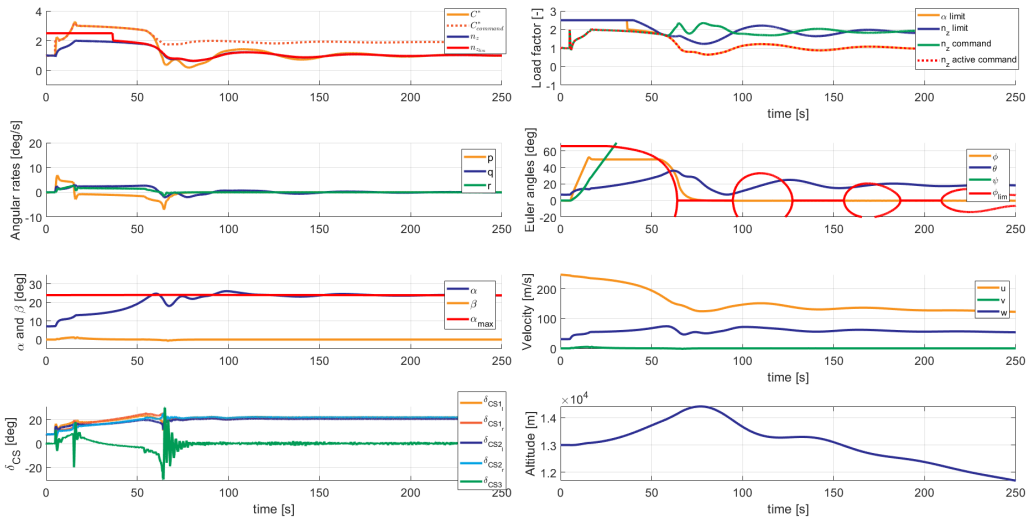

Fig. 20 Flight Envelope Protection starting from cruise height, with roll

altitude of 1 km, with the roll rate input. It should be kept in mind that the simulation time is 100 s instead of 250, as the aircraft reaches the angle of attack limit faster in this condition. The pitch angle goes below zero twice, instead of only once. The rudder oscillation in this case seems to have a lower frequency, but higher amplitude. The oscillations occur at an airspeed of around 50 m/s, which could be resolved by scheduling gains for this low velocity. Because of the lower starting airspeed, the roll limits already limits the roll, when there is still an roll input. The controller is able to deal with this, even though the rudder, as well as two control surfaces are at their saturation limit during this period, indicating that the aircraft is at its limit for this manoeuvre. The angle of attack during this period is not getting above 30 degrees and the roll angle is getting to zero, this however takes more time, then for the cruise condition time, which can be explained by the fact that the control surfaces are at their limit. And while the rudder is also at its saturation limit, the sideslip angle is not becoming to large.

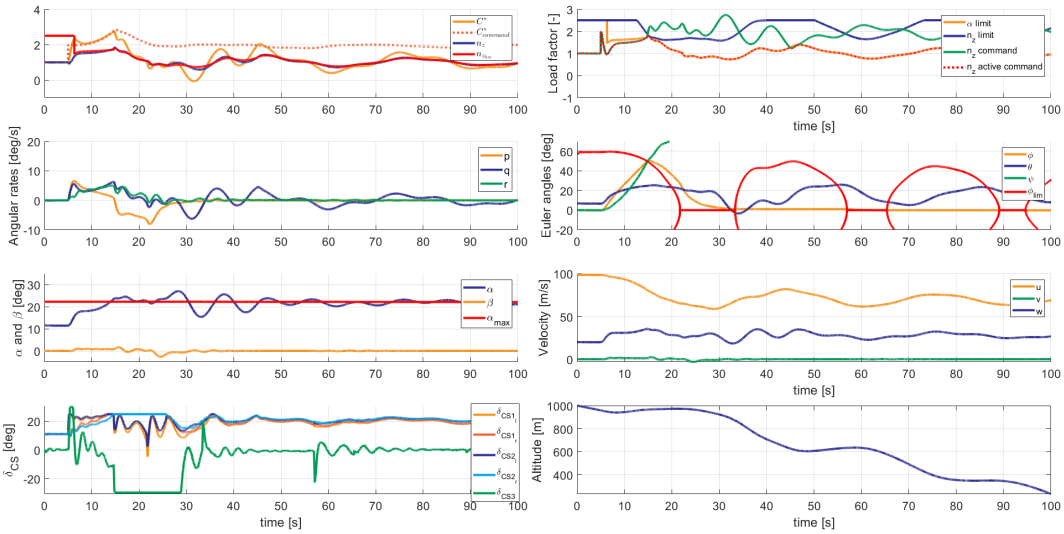

Fig. 21 Flight Envelope Protection starting from from 1 km altitude, with roll

VI. Conclusion

In this research a Flight Control System for the Flying-V is proposed. The FCS is based on an innerloop INDI control law, with a C^* control law for longitudinal control and a Rate Control Attitude Hold control law for roll. It is shown that this controller can be tuned to be within Level 1 Handling Qualities, for the selected cruise and approach conditions. When sensor dynamics and discrete effects are taken into account, the gain and phase margins decreases. As long as the body rate sensor is fast enough, the FCS can still be tuned into level 1 handling qualities. The effect of sampling frequency is evaluated, and a sampling frequency of 100 Hz is fast enough to not introduce extra tracking errors. It is also shown that the FCS is robust to aerodynamic uncertainties, as the response does not change much for differences in aerodynamic parametersup to 20 %.

Finally the Flight Envelope Protection is evaluated. For the cases evaluated, the angle of attack stays under the set limit of 30 degrees. As the FEP only activates for higher angles of attack, and when the roll angle is close to its limit, it also does not influence the aircraft response when well within its flight envelope. Lastly the load factor does not exceeds the limits meaning that the FEP meets all the requirements that were set, for the cases that are tested.

However there are some factors that should be further investigated. This research only looks at one position of the c.g. of the aircraft, which is also perfectly known. Further research could investigate the effects of changing c.g. location, as well as c.g. location mismatch. The Flight Envelope protection could also be improved, by for example also take the angle of attack rate into account, making the angle of attack protection more gradual, and possibly being able to make the maximum angle of attack larger. The minimum angle of attack and load factor protection laws are also not tested yet. Another improvement that could be done is adding a V_{max} and V_{min} protection.

There are also other effects that could degrade the performance of the control laws, that are not taken into account yet. These are for example aero-elasticity effects, which could have a big impact on the controllers performance, and time delay within the flight control computer.

It should also be investigated if improving the gain scheduling, and making it also dependant on the air density, is enough to reduce the rudder oscillations, or that the lateral control authority should be increased in another way. Lastly it could be investigated if the required sensors in this research are feasible for the Flying-V, or that the control laws should be changed, to control laws that are less sensitive for time delays induced by the sensors, to ensure enough gain and phase margin.

References

[1] Lee, D., Pitari, G., Grewe, V., Gierens, K., Penner, J., Petzold, A., Prather, M., Schumann, U., Bais, A., Berntsen, T., Iachetti, D., Lim, L., and Sausen, R., "Transport impacts on atmosphere and climate: Aviation," *Atmospheric Environment*, Vol. 44, No. 37, 2010, pp. 4678–4734. https://doi.org/10.1016/j.atmosenv.2009.06.005, transport Impacts on Atmosphere and Climate: The ATTICA Assessment Report.

[2] Faggiano, F., "Aerodynamic Design Optimization of a Flying V Aircraft," Master's thesis, TU Delft, 2016. URL http://resolver.tudelft.nl/uuid:0b1472a5-3aad-433c-9a64-242c84b114fd.

[3] Benad, J., "The Flying V - A new Aircraft Configuration for Commercial Passenger Transport," *Deutscher Luft- und Raumfahrtkongress 2015, Rostock*, Deutsche Gesellschaft für Luft- und Raumfahrt, 2015. https://doi.org/10.25967/370094.

[4] Palermo, M., "The Longitudinal Static Stability and Control Characteristics of a Flying V Scaled Model," Master's thesis, TU Delft, 2019. URL http://resolver.tudelft.nl/uuid:6286f9e2-c24a-430c-a4fa-9fb67b9558b4.

[5] Cappuyns, T., "Handling Qualities of a Flying V Configuration," Master's thesis, TU Delft, 2019. URL http://resolver.tudelft.nl/uuid:69b56494-0731-487a-8e57-cec397452002.

[6] Horwitz, J., "Parametric Design of the Flying-V Winglets for Improved Lateral-Directional Stability and Control," Master's thesis, TU Delft, 2021. URL http://resolver.tudelft.nl/uuid:d7513b36-b9fd-4f8a-8726-f5c7ee7f3a6b.

[7] van Overeem, S., "Modelling, Control, and Handling Quality Analysis of the Flying-V," Master's thesis, TU Delft, 2021. URL http://resolver.tudelft.nl/uuid:7fd04eec-41d4-4967-b246-89fdfac2446e.

[8] Smith, P., "A simplified approach to nonlinear dynamic inversion based flight control," *23rd Atmospheric Flight Mechanics Conference*, American Institute of Aeronautics and Astronautics, 1998. https://doi.org/10.2514/6.1998-4461.

[9] Wang, X., van Kampen, E.-J., Chu, Q., and Lu, P., "Stability Analysis for Incremental Nonlinear Dynamic Inversion Control," *Journal of Guidance, Control, and Dynamics*, Vol. 42, No. 5, 2019, pp. 1116–1129. https://doi.org/10.2514/1.G003791.

[10] Sieberling, S., Chu, Q. P., and Mulder, J. A., "Robust Flight Control Using Incremental Nonlinear Dynamic Inversion and Angular Acceleration Prediction," *Journal of Guidance, Control, and Dynamics*, Vol. 33, No. 6, 2010, pp. 1732–1742. https://doi.org/10.2514/1.49978, URL https://doi.org/10.2514/1.49978.

[11] van Overeem, S., Wang, X., and Kampen, E.-J. V., "Modelling and Handling Quality Assessment of the Flying-V Aircraft," *MST-05, Modeling and Simulation of Air and Space Vehicle Dynamics, Systems, and Environments I, January 4*, AIAA SciTech 2022, 2021. https://doi.org/10.2514/6.2022-1429.

[12] Garcia, A. R., Vos, R., and de Visser, C., "Aerodynamic Model Identification of the Flying V from Wind Tunnel Data," *AIAA AVIATION 2020 FORUM*, 2020. https://doi.org/10.2514/6.2020-2739.

[13] Matamoros, I., and de Visser, C. C., "Incremental Nonlinear Control Allocation for a Tailless Aircraft with Innovative Control Effectors," *2018 AIAA Guidance, Navigation, and Control Conference*, AIAA, 2018. https://doi.org/10.2514/6.2018-1116, URL https://arc.aiaa.org/doi/abs/10.2514/6.2018-1116.

[14] European Union Aviation Safety Agency, "Type-Certificate Data Sheet No. E.111 for Trent XWB Series Engines," , 2019. URL https://www.easa.europa.eu/document-library/type-certificates/engine-cs-e/easae111.

[15] van 't Veld, R., Kampen, E.-J. V., and Chu, Q. P., "Stability and Robustness Analysis and Improvements for Incremental Nonlinear Dynamic Inversion Control," *2018 AIAA Guidance, Navigation, and Control Conference*, 2018. https://doi.org/10.2514/6.2018-1127, URL https://arc.aiaa.org/doi/abs/10.2514/6.2018-1127.

[16] Stevens, B. L., Lewis, F. L., and Johnson, E. N., *Aircraft Control and Simulation: Dynamics, Controls Design, and Autonomous Systems*, John Wiley & Sons, Ltd, 2015. https://doi.org/https://doi.org/10.1002/9781119174882.ch7.

[17] Grondman, F., Looye, G., Kuchar, R. O., Chu, Q. P., and Kampen, E.-J. V., "Design and Flight Testing of Incremental Nonlinear Dynamic Inversion-based Control Laws for a Passenger Aircraft," *2018 AIAA Guidance, Navigation, and Control Conference*, AIAA, 2018. https://doi.org/10.2514/6.2018-0385, URL https://arc.aiaa.org/doi/abs/10.2514/6.2018-0385.

[18] Li, M., Li, J., Tang, Y., and Sun, S., "An Extended INDI Approach and Application to Pitch Rate Control Laws Design of an Aircraft," *AIAA AVIATION 2021 FORUM*, AIAA, 2021. https://doi.org/10.2514/6.2021-3005.

[19] Durham, W., Bordignon, K. A., and Beck, R., *Aircraft Control Allocation*, John Wiley & Sons, 2017. URL https://app.knovel.com/hotlink/khtml/id:kt011B38E1/aircraft-control-allocation/direct-allocation.

[20] Lombaerts, T., Looye, G., Ellerbroek, J., and Martin, M. R. y., "Design and Piloted Simulator Evaluation of Adaptive Safe Flight Envelope Protection Algorithm," *Journal of Guidance, Control, and Dynamics*, Vol. 40, No. 8, 2017, pp. 1902–1924. https://doi.org/10.2514/1.G002525.

[21] Favre, C., "Fly-by-wire for commercial aircraft: the Airbus experience," *International Journal of Control*, Vol. 59, No. 1, 1994, pp. 139–157. https://doi.org/10.1080/00207179408923072.

[22] Delannoy, S., and Oudin, S., "Longitudinal control law for modern long range civil aircrafts," *EuroGNC 2013, 2nd CEAS Specialist Conference on Guidance, Navigation & Control*, 2013. URL https://aerospace-europe.eu/media/books/delft-0027.pdf.

[23] Smeur, E. J. J., Chu, Q., and de Croon, G. C. H. E., "Adaptive Incremental Nonlinear Dynamic Inversion for Attitude Control of Micro Air Vehicles," *Journal of Guidance, Control, and Dynamics*, Vol. 39, No. 3, 2016, pp. 450–461. https://doi.org/10.2514/1.G001490.

[24] Oudin, S., "Low Speed Protections for a Commercial Airliner : a Practical Approach," *AIAA Guidance, Navigation, and Control Conference*, American Institute of Aeronautics and Astronautics, 2017. https://doi.org/10.2514/6.2017-1023.

[25] Department of Defense, *MIL-STD-1797A, FLYING QUALITIES OF PILOTED AIRCRAFT*, 1990.

[26] Mansur, M. H., Lusardi, J. A., Tischler, M. B., and Berger, T., "Achieving the Best Compromise between Stability Margins and Disturbance Rejection Performance," *American Helicopter Society 65th Annual Forum*, 2009.

[27] Cook, M. V., *Flight Dynamics Principles: A Linear Systems Approach to Aircraft Stability and Control*, Butterworth-Heinemann, 2013. https://doi.org/10.1016/C2010-0-65889-5.

[28] Falkena, W., "Investigation of practical flight control systems for small aircraft," Ph.D. thesis, TU Delft, 2012. https://doi.org/10.4233/uuid:22554e85-9506-4410-9fb3-9ad6af4b2c8d.

[29] Hodgkinson, J., and Lamanna, W., "Equivalent system approaches to handling qualities analysis and design problems of augmented aircraft," *Guidance and Control Conference*, McDonnel Aircraft Company, 1977. https://doi.org/10.2514/6.1977-1122.

[30] Gibson, J., "Development of a design methodology for handling qualities excellence in fly by wire aircraft," Ph.D. thesis, TU Delft, 1999. URL http://resolver.tudelft.nl/uuid:6b564b35-cb74-436c-8c47-845bfbbb8b4d.

[31] Mitchell, D. G., Hoh, R. H., Aponso, B. L., and Klyde, D. H., "Proposed Incorporation of Mission-Oriented Flying Qualities into MIL-STD-1797A." 1994.

[32] Lambregts, A. A., "Flight Envelope Protection for Automatic and Augmented Manual Control," *Proceedings of the EuroGNC 2013, 2nd CEAS Specialist Conference on Guidance, Navigation & Control*, Council of European Aerospace Societies (CEAS), 2013, pp. 1364–1383.

[33] Puyou, G., and Losser, Y., "Clearance Benchmark for a Civil Aircraft," *Optimization Based Clearance of Flight Control Laws: A Civil Aircraft Application*, edited by A. Varga, A. Hansson, and G. Puyou, Springer Berlin Heidelberg, Berlin, Heidelberg, 2012, pp. 11–36. https://doi.org/10.1007/978-3-642-22627-4_2, URL https://doi.org/10.1007/978-3-642-22627-4_2.